

DR 21 South Filament: a Parsec-sized Dense Gas Accretion Flow onto the DR 21 Massive Young Cluster

BO HU,^{1,2} KEPING QIU,^{1,2} YUE CAO,^{1,2} JUNHAO LIU,^{1,2} YUWEI WANG,^{1,2} GUANGXING LI,³
ZHIQIANG SHEN,^{4,5} JUAN LI,⁴ JUNZHI WANG,⁴ BIN LI,⁴ AND JIAN DONG⁴

¹*School of Astronomy and Space Science, Nanjing University, 163 Xianlin Avenue, Nanjing 210023, China*

²*Key Laboratory of Modern Astronomy and Astrophysics (Nanjing University), Ministry of Education, Nanjing 210023, China*

³*South-Western Institute for Astronomy Research, Yunnan University, Kunming, 560500 Yunnan, China*

⁴*Shanghai Astronomical Observatory, 80 Nandan Road, Shanghai 200030, China*

⁵*Key Laboratory of Radio Astronomy, Chinese Academy of Sciences, People's Republic of China*

Submitted to ApJ

ABSTRACT

DR21 south filament (DR21SF) is a unique component of the giant network of filamentary molecular clouds in the north region of Cygnus X complex. Unlike the highly fragmented and star-forming active environment it resides, DR21SF exhibits a coherent profile in the column density map with very few star formation signposts, even though the previously reported linear density of the filament is an order of magnitude higher than the thermal stable threshold. We derive the size (3.6 pc by 0.13 pc), temperature (10 to 15 K), and mass (1048 M_{\odot}) of DR21SF from Shanghai 65 m TianMa Radio Telescope (TMRT) observations of NH₃ (1, 1) and (2, 2) inversion lines in conjunction with the column density map from our previous work. Star-forming sites are identified along the filament where gas temperature excesses. We find clear gradients in radial velocity and intrinsic line-width along the spine of the filament. The gradients can be well interpreted with a scenario of an accretion flow feeding DR 21 at a mass transfer rate of $1.1 \times 10^{-3} M_{\odot} \text{ yr}^{-1}$. Based on the analysis of its kinematic temperature, intrinsic line-width and mass distribution, we conclude that DR21SF is in an overall trans-critical status, which indicates an early evolutionary stage.

Keywords: ISM: molecules — ISM: structure — radio lines: ISM

1. INTRODUCTION

Understanding how stars, especially massive stars ($M > 8 M_{\odot}$), arise from the interstellar medium (ISM) has long been a major challenge

in modern astrophysics. Even though the relationship between filaments and star formation activities in molecular clouds has been proposed by both theoretical (e.g., Ostriker 1964; Inutsuka & Miyama 1992) and observational (e.g., Schneider & Elmegreen 1979) works for decades, it was the studies based on *Herschel* Space Ob-

servatory (e.g., Miville-Deschênes et al. 2010; Henning et al. 2010) that ultimately demonstrated the ubiquitous presence of filaments in the star-forming activities. Filamentary structures in molecular clouds are found to fragment into nodes with scales from 0.01 to 0.1 pc in a gravitationally unstable status (André et al. 2010). These nodes are candidates to form low-/intermediate-mass stars or star clusters (e.g., Johnstone & Bally 1999), while in some cases they can be as massive as several hundred solar masses, and are capable of forming massive stars or star clusters (e.g., Jackson et al. 2010; Mattern et al. 2018). There are also scenarios of a high-mass star forming region (HMSFR) connected to one (the “head-tail” scenario Tachihara et al. 2002) or more (the “hub-like” system Myers 2009) filaments. In these filaments, flows of gas that converge to the HMSFR caused by longitudinally collapse may exist (Liu et al. 2012; Peretto et al. 2013; Lu et al. 2018). The accretion flow along the filament is proposed to be a more efficient mechanism than an isotropic accretion to prolong the accretion time for the high-mass star forming cores to gain their mass (Myers 2009).

The Cygnus X giant molecular cloud complex offers a large sample of star formation regions which show diversities in both physical conditions and evolutionary stages. Thus, it is known as an excellent laboratory for studying the star formation process. Lying $1.50_{-0.07}^{+0.08}$ kpc (Rygl et al. 2012) away, the DR 21 ridge, consisting of DR21(OH) and DR 21, is the most massive and star-forming active filament in the Cygnus X complex. In the northern part of the ridge, lies the DR21(OH), which is an extremely massive ($34000 M_{\odot}$, Schneider et al. 2010) star-forming region with intensive maser activities (Kogan & Slysh 1998; Harvey-Smith et al. 2008). Schneider et al. (2010) find out that three sub-filaments (F1, F2, F3) are directly linked to DR21(OH), showing apparent veloc-

ity gradients along their spines and suggesting material flows towards DR21(OH) (Hennemann et al. 2012, hereafter, H12). To the south resides the relatively more evolved massive star forming region DR 21. It harbors a group of luminous H II regions (Cyganowski et al. 2003) and massive protostars traced by Class I and II methanol masers (e.g., Kogan & Slysh 1998; Rygl et al. 2012). DR 21 is also well-known by being associated with the most luminous ($1800 L_{\odot}$) and massive ($>3000 M_{\odot}$) outflow in the Galaxy (Garden et al. 1986; Davis et al. 2007). Two filamentary structures (referred as S filament and SW filament by H12) attached to DR 21 have been identified in the column density map. The more prominent one, S filament, is referred as DR 21 South Filament (DR21SF, see Figure 1) in this work, and extends about $8'$ directly from DR 21 to the south.

From a larger perspective, a network of dense gas filaments in the northern part of Cygnus X is associated with all the major massive star forming regions (e.g., DR 22, DR 23, W75N, DR 21, DR 17) in the area (Schneider et al. 2010; Cao et al. 2019, hereafter, Cao19). This network hosts a number of filaments, most of which are overall fragmented and showing rich signposts of star formation. In contrast, DR21SF exhibits a coherent profile in the column density map, and only sparse star formation candidates are found (e.g., Kryukova et al. 2014) towards it. H12 reported an average linear mass of $500 M_{\odot} \text{ pc}^{-1}$ for this filament, which is an order of magnitude higher than the typical thermal critical linear mass, $10 M_{\odot} \text{ pc}^{-1}$ (Arzoumanian et al. 2013). Based on observations towards several nearby filaments, Arzoumanian et al. (2013) concluded that super-critical filaments should fragment into cores and the subsequent local core collapse occurs faster than global cloud collapse and thus super-critical filaments should be highly fragmented. However, DR21SF seems to be distinct from the above scenario.

This filament has also been detected by Schneider et al. (2006) in ^{13}CO 2 \rightarrow 1, with a radial velocity ranges from -6 km s^{-1} to -1 km s^{-1} . It shows roughly a radial velocity gradient from south to north in the channel map, which is often seen in the filaments that connecting to HMSFRs. The possibility of analyzing the physical status of DR21SF is limited by the spatial resolution of their data ($130''$). In order to understand the nature of DR21SF and its relationship with the DR 21, we perform spectral line observations of NH_3 towards the filament, which will be analyzed in conjunction with our existing column density map of the filament derived from the *Herschel* data. The NH_3 transitions $(J, K) = (1, 1)$ and $(2, 2)$ trace gas with densities of $\sim 10^4 \text{ cm}^{-3}$ (Rohlfs & Wilson 2004) with a wide range of excitation temperatures (Ho & Townes 1983). Unlike ^{13}CO , which is not sensitive to gas with density larger than 10^3 cm^{-3} , NH_3 has been commonly used as an exclusive probe of cold dense gas in star-forming molecular clouds. We therefore carry out single-dish observations of NH_3 $(1, 1)$ and $(2, 2)$ transitions toward DR21SF using Shanghai 65 m TianMa Radio Telescope (TMRT), trying to connect the internal gas kinematics of the filament with its unique column density profile.

In Section 2, we present technical details of the observations and the data; The observational results and derived parameters of DR21SF are presented in Section 3; In Section 4, we will discuss the stability and kinematics of DR21SF and propose an accelerating in-fall gas flow scenario for the filament.

2. OBSERVATIONS AND DATA

2.1. Dust Continuum Emission Data

In order to derive the mass distribution of DR21SF, we adopt the column density map of Cygnus X complex from Cao19. *Herschel* PACS ($160 \mu\text{m}$) and SPIRE (250 , 320 , and

$500 \mu\text{m}$) images are employed in the spectral energy distribution (SED) fitting to produce the column density map with an angular resolution of $18''$. Detailed description about how the column density map is derived can be found in Cao19. One should notice that the SED fitting in Cao19 did not include the PACS $70 \mu\text{m}$ data since the emission at this wavelength arises from warm dust and a single temperature model is no longer applicable. Given that the filament is overall quiescent and at low temperature, the estimate of the column density would not be significantly affected by neglecting the $70 \mu\text{m}$ data.

2.2. Ammonia Emission Line Observations

We carry out observations of NH_3 $(1, 1)$ and $(2, 2)$ lines towards DR21SF in both on-the-fly (OTF) and point by point On-Off modes with Tianma 65 m telescope to obtain both a position-position-velocity data cube covering the whole filament, and high resolution spectra of targeted positions. The total bandwidth of 500 MHz (OTF mode) and 187 MHz (On-Off mode) are split into two sub-bands centered at 23694.4955 MHz and 23722.6333 MHz with frequency resolutions of 30.517 kHz (OTF mode) and 5.722 kHz (On-Off mode), respectively, corresponding to velocity resolutions of 0.39 km s^{-1} (OTF mode) and 0.07 km s^{-1} (on-off mode). The FWHM beam-size is about $48''$.

In the OTF observations, we map an area of $4.5'$ by $9.0'$ covering DR21SF on 25/11/2017, 07/02/2018 and 09/02/2018. The average system temperature of the observations in three days is about 70 K . The nominal integration time on each sampled point is about 3 minutes in total. Only the main component of NH_3 $(1, 1)$ is detected in the OTF observations because the filament is overall faint in NH_3 emission and the effective integration time is limited for such a large OTF map. The final data cube is then produced by combining all data with weights inversely proportional to their system tempera-

tures, and re-gridding the image to a pixel size of $16''$, approximately one third of the beam-size.

The On-Off observations are made with a long integration time of 10 minutes towards each target position. We observe a total of 10 positions along the spine of DR21SF with spacings approximately identical to the beam-size, to cover the entire filament. We name these ten positions as P01 to P10 from north to south. We fit all the observed NH_3 (1, 1) profiles with a five-component model, whereas (2, 2) transition line profiles with single Gaussian model since we fail to detect the satellite lines of this transition.

3. RESULT

3.1. Morphology and Mass

On the column density map, DR21SF is connected to DR 21 at its northern end, and extends $\sim 8'$ to the southeast. Since DR21SF and DR 21 have similar radial velocities (about -3 km s^{-1}), it is reasonable to infer that these two structures are physically associated with each other. We therefore adopt trigonometric parallax distance of $1.50_{-0.07}^{+0.08}$ kpc of DR 21 (Rygl et al. 2012) for DR21SF, which leads to a length of 3.6 pc, given an inclination angle of 18° (see discussion in Section 4.2). The width of DR21SF is derived by fitting the averaged column density profile perpendicular to the spine of the filament. We only employ the transverse column density profiles at P03 to P09 for the width estimation, since the column densities in the middle segment of the filament are consistent. The asymmetry of the averaged transverse column density profile (see Figure 2) is caused by the clump DR21-10 (identified by Cao19), which is on the east side of DR21SF and about 0.7 pc away from the spine of the filament. According to the cylinder model of an infinite gas filament (e.g., Ostriker 1964; Arzoumanian et al. 2011), whose radial volume density follows

$$\rho(r) = \frac{\rho_c}{[1 + (r/r_0)^2]^{p/2}} \quad (1)$$

the transverse column density can be described as a Plummer-like function:

$$N(r) = A_p \frac{\rho_c \sqrt{8} r_0}{(1 + \frac{r^2}{8r_0^2})^{(p-1)/2}}, \quad (2)$$

where $A_p = \frac{1}{\cos \theta} \int \frac{du}{(1+u^2)^{p/2}}$, θ is the inclination and set to 18° , ρ_c is the central volume density of the filament, r_0 is the scale radius representing the flat distribution of the density at the spine of the filament. We fit the average transverse column density \bar{N}_{trans} profile with this model. Shown in the lower panel of Figure 2, the best fit, which gives a minimum χ^2 , results in $p = 1.7 \pm 0.1$, $\rho_c = (1.6 \pm 0.2) \times 10^4 \text{ cm}^{-3}$ and $r_0 = (4.2 \pm 0.6) \times 10^{-2} \text{ pc}$. The errors are of one-sigma uncertainties. The derived p value is in agreement with that found in filaments such as IC 5146 ($1.5 < p < 2.5$, Arzoumanian et al. 2011) and Serpens South filament ($p = 1.9 \pm 0.2$, Kirk et al. 2013). The central density ρ_c of DR21SF is significantly lower than that of several other star-forming filaments (see Table 3 of Gong et al. 2018). When $p \approx 2$ the FWHM of the radial column density profile of the gas cylinder is about $3 \times r_0$ (Arzoumanian et al. 2011), thus we estimate the width of DR21SF as 0.13 pc. This result seems in good agreement with the 0.1 pc ‘‘universal’’ width of filaments in molecular clouds in the solar neighborhood proposed by Arzoumanian et al. (2011). However, the resolution of the column density map we used is $18''$, which corresponds to 0.13 pc at a distance of 1.5 kpc. We think the width estimation is limited by this resolution, even though the fitting is performed on the column density profile, whose FWHM is significantly larger than the resolution.

The mass of DR21SF can be estimated from the column density map by

$$M = \sum N_i \mu m_H A_i, \quad (3)$$

where N_i is the column density of the i -th pixel on column density map within the area of the filament, μ is the average molecular weight, m_H is

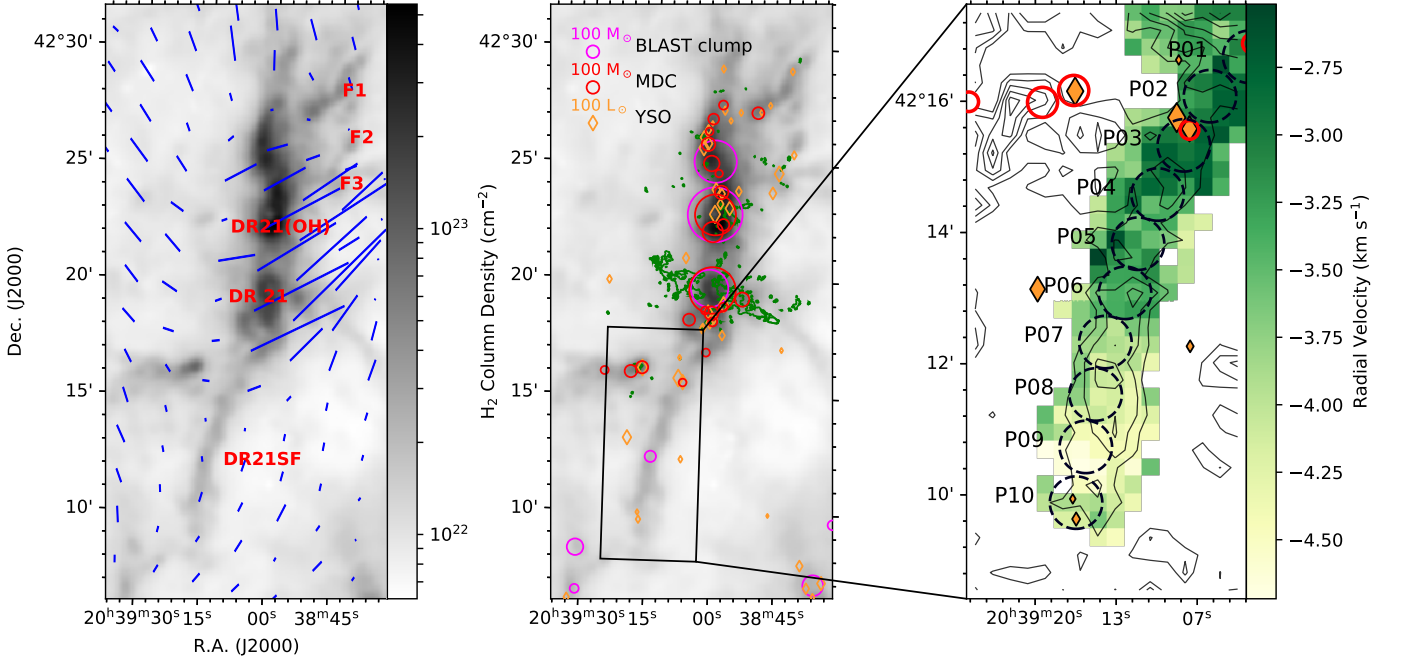


Figure 1. *Left panel:* The column density of the DR 21 area is shown by gray scale. The orientation of the blue segments indicates the orientation of the the magnetic field traced by polarized dust emission and length of the segments indicates the relative fraction of polarization. *Middle panel:* The gray scale is the same as the left panel. Red and magenta circles denote the MDCs (massive dense cores) with mass greater than $35 M_{\odot}$ recognized by Cao19 and clumps discovered by BLAST FIR observation, respectively, with the diameter proportional to their mass. YSOs are denoted with orange diamond (open in left panel, and filled in right panel), with the side length proportional to $\log L_{\text{YSO}}$, where L_{YSO} is the luminosity of the YSO. Scales of MDC and BLAST clump with mass of $100 M_{\odot}$ and YSO with luminosity of $100 L_{\odot}$ are shown in the upper left corner. Outflows identified by $2.122 \mu\text{mH}_2$ emission are marked with green contours. *Right panel:* The contour and the color map indicates the moment-0 and moment-1 map of NH_3 (1, 1) emission along DR21SF, respectively. Black dashed circles indicate the beam-sizes and positions of 10 pointed observations. The MDCs, BLAST clumps, and YSOs shown in the middle panel are also marked in this panel with corresponding marker and scale.

the mass of a hydrogen atom, and A_i is the area of the i -th pixel at the distance of the source. We calculate the total mass within an area of a stripe along the spine of the filament with a width of 0.75 pc, which is the total width of the best-fit transverse column density profile above the typical background level ($1 \times 10^{22} \text{cm}^{-2}$). With $\mu = 2.8$, a total mass of $1048 M_{\odot}$ is derived. Cao19 estimates the average relative uncertainty of column density to be about 40% in the area of DR21SF. Considering the distance uncertainty is about 5%, we claim that the uncertainty of the total mass is 50%.

The mass we estimated is smaller than that ($1350 M_{\odot}$) proposed by H12, even though their result is within the uncertainty of ours. The discrepancy mainly comes from the systematic difference in the column density maps produced by H12 and Cao19. As a comparison, the column densities of the densest region in DR 21 and the nearby least dense regions reported by Cao19 are about $1.5 \times 10^{23} \text{cm}^{-2}$ and $7.0 \times 10^{21} \text{cm}^{-2}$, respectively, whereas H12 presents corresponding values of $> 1.0 \times 10^{24} \text{cm}^{-2}$ and $\sim 1.0 \times 10^{22} \text{cm}^{-2}$, respectively. The systematic difference can be explained by their data reduction approach. The SED fitting performed by Cao19 is

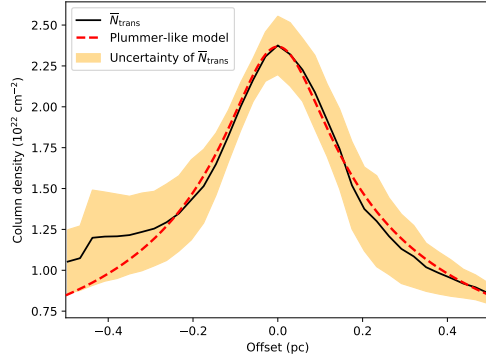


Figure 2. The averaged transverse column density (\bar{N}_{trans}) is calculated within a stripe of 1 pc wide long the spine of the filament on the column density map. \bar{N}_{trans} profile and its uncertainty are denoted by the black line and the yellow belt, while the red dashed line represents the best-fit Plummer-like model.

based on images of 160 μm , 250 μm , 350 μm , and 500 μm , whereas H12 does not include the data of 500 μm . The long wavelength data is essential to the SED fitting of cold gas. For example, with a temperature of 15 K, the SED peaks at a wavelength of 340 μm . Thus, data at 500 μm will certainly help improve the SED fitting of the cold gas in DR21SF. The discrepancy should effect both the mass and the temperature measurements as they are direct results from the SED fitting. We do find a systematic difference about 3 K in the dust temperature of DR21SF between H12 and Cao19 as well. A column density about $1.2 \times 10^{23} \text{ cm}^{-2}$ was independently derived from the archive data of European Space Agency’s Infrared Space Observatory (ISO) Long-Wavelength Spectrometer (LWS) by Jakob et al. (2007) towards the densest region in DR 21. This value is in good agreement with that of Cao19. We therefore conclude that the column density map presented by Cao19 is a better estimate compared to that by H12, therefore is adopted in this work for the mass calculation. We also noticed that both of these two SED fitting processes did not take

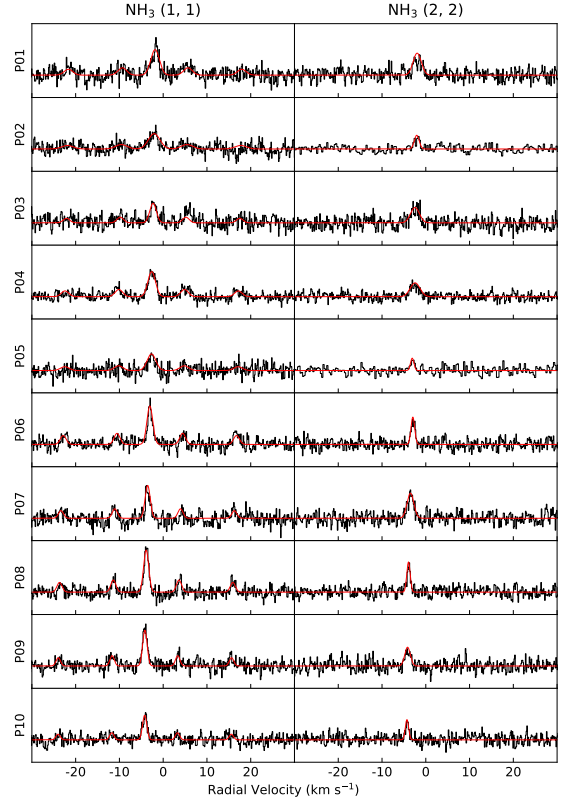


Figure 3. From top to bottom are the NH_3 (1, 1) (left column) and (2, 2) (right column) line profile of P01 to P10. Black lines indicate the data, whereas the red lines illustrate the best fit models.

into account the 70 μm data. The dust emission at 70 μm mainly traces the warm gas component in the molecular clouds thus may introduce extra uncertainty to the SED if only a single temperature component of cold gas is applied in the fitting. Neglecting the warm gas component traced by shorter wavelength emission will certainly underestimate the total mass of molecular clouds, especially for molecular clouds with high star formation rates. However, DR21SF shows very few star formation signposts (see discussion in Section 4.1 below), therefore, we think this effect is neglectable compared to other sources of uncertainty in the estimation of the total mass.

3.2. Optical Depth and Gas Temperature

Data from the On-Off observations towards P01 to P10 are used to derive the optical depth and gas temperature of the DR21SF. In Figure 3, the line profiles of both NH_3 (1, 1) and (2, 2) transitions at P01 to P10 are presented. To improve the SNR, we perform Hanning smoothing to the original data, and it results in an effective velocity resolution of 0.15 km s^{-1} . With assumptions of equal beam-filling factor and equal excitation temperature for each hyper-fine transition, and a cosmic background temperature of 2.7 K, we use the CLASS package of the GILDAS¹ software to fit the NH_3 (1, 1) line profiles. We only perform simple Gaussian fitting to the NH_3 (2,2) lines, since we only detect the main component of this transition. Derived parameters are listed in Table 1. We follow Equation 4 in Ho & Townes (1983) to calculate rotational temperature (T_{rot}). Since NH_3 (1, 1) and (2, 2) transitions are not sensitive to temperatures significantly higher than 30 K (e.g., Lu et al. 2014), the $T_{\text{rot}} \gtrsim 30 \text{ K}$ derived with this method can only be treated as a lower limit. Based on T_{rot} we are able to calculate the kinematic temperature (T_{kin}), by applying the empirical relationship introduced by Walmsley & Ungerechts (1983):

$$\frac{1}{T_{\text{rot}}} = \frac{1}{T_{\text{kin}}} + \frac{1}{41.5} \ln[1 + 0.6 \exp - \frac{15.7}{T_{\text{kin}}}] \quad (4)$$

Both T_{kin} and T_{rot} for each position are also given in Table 1.

3.3. Velocity and Line-width

The radial velocities along DR21SF with respect to local standard of rest (LSR) range from -4.23 to -1.85 km s^{-1} . In the right panel of Figure 1, we present the first moment map of the filament. From both the first moment map and the radial velocities presented in Table 1 one can easily see a gradient in radial velocity along the

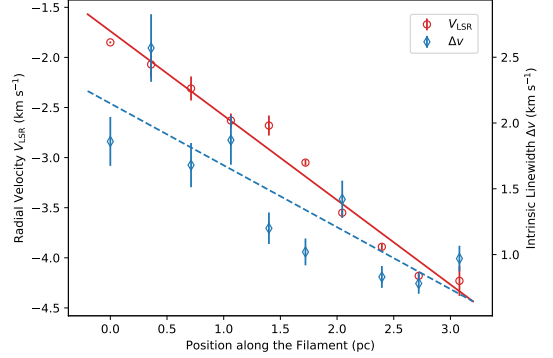


Figure 4. The red circles and solid line indicate the data and the best-fit linear model of radial velocity, while blue diamonds and dashed line indicate the intrinsic line-width and its best-fit linear model.

filament. In Figure 4, we plot the radial velocity as a function of the position along the filament with respect of P01. The radial velocities are well characterized by the linear model, which gives a gradient of $(0.8 \pm 0.1) \text{ km s}^{-1} \text{ pc}^{-1}$. This value is comparable to that in other similar filamentary molecular clouds, e.g., $0.7 \text{ km s}^{-1} \text{ pc}^{-1}$ in Orion filament (Bally et al. 1987), $0.15\text{-}0.6 \text{ km s}^{-1} \text{ pc}^{-1}$ in SDC13 (Peretto et al. 2014), $0.8\text{-}2.3 \text{ km s}^{-1} \text{ pc}^{-1}$ in DR21(OH) (Schneider et al. 2010). Moreover, a decreasing can also be seen in the intrinsic line-width along the filament from north to south. We again apply a linear model to give a first order estimate of such a gradient. The best-fit result reads $(0.5 \pm 0.1) \text{ km s}^{-1} \text{ pc}^{-1}$.

Due to the limited spectral resolution, the line-width directly derived from the observed line profile is the true line-width of the emission (intrinsic line-width) convolved with an instrumental spectral resolution and blurred with adjacent hyper-fine structures. Also, the radial velocity gradient along the filament will broaden the measured line-width when observed with a certain beam-size. To eliminate these effects, we first subtract the instrumental spectral resolution and contribution of velocity gradient within

¹ <https://www.iram.fr/IRAMFR/GILDAS/>

Table 1. Physical properties of NH₃ along the DR 21 south filament.

Position	R.A.	Dec.	T_{rot}	T_{kin}	$\tau(1, 1)$	V_{lsr}	ΔV_{fit}	ΔV_{int}	\mathcal{M}_{1D}
	($^{\circ}$)	($^{\circ}$)	(K)	(K)		(km s $^{-1}$)	(km s $^{-1}$)	(km s $^{-1}$)	
P01	309.760	42.278	10.9	11.3	0.11	-1.85 \pm 0.01	1.98 \pm 0.14	1.86	10.18
P02	309.773	42.268	21.4	25.0	0.10	-2.07 \pm 0.13	2.63 \pm 0.37	2.57	9.45
P03	309.782	42.255	>30.4	>40.6	0.10	-2.31 \pm 0.12	1.81 \pm 0.42	1.68	4.83
P04	309.791	42.243	12.1	12.7	0.10	-2.63 \pm 0.07	1.99 \pm 0.16	1.87	9.66
P05	309.798	42.230	10.4	10.8	0.10	-2.68 \pm 0.10	1.34 \pm 0.27	1.20	6.71
P06	309.803	42.218	9.7	10.0	0.10	-3.05 \pm 0.03	1.17 \pm 0.08	1.02	5.93
P07	309.809	42.206	>38.3	>58.8	0.10	-3.55 \pm 0.03	1.56 \pm 0.12	1.42	3.39
P08	309.813	42.192	22.1	26.1	0.10	-3.89 \pm 0.03	1.02 \pm 0.09	0.83	2.96
P09	309.816	42.179	14.2	15.2	0.10	-4.18 \pm 0.04	0.98 \pm 0.10	0.78	3.66
P10	309.819	42.165	22.3	26.3	0.10	-4.23 \pm 0.15	1.13 \pm 0.20	0.97	3.46

NOTE—The right ascension and declination are of J2000. T_{rot} and T_{kin} are the rotational and kinematic temperature, respectively. $\tau(1, 1, m)$ denotes the optical depth of the NH₃ (1, 1) transition. The ΔV_{fit} and ΔV_{int} stand for the fitted (“blend”) and intrinsic line-width, and the one dimensional Mach is listed in the last column.

the beam-size (0.3 km s $^{-1}$ in our case) quadratically from the measured line-width to derive a “blurred” line-width. We then follow the empirical relation (Barranco & Goodman 1998) between the intrinsic and the “blurred” line-width to estimate the former. Results are listed in Table 1. We evaluate the uncertainty of intrinsic line-width to be 12%, since the average one-sigma uncertainty of fitted line-width is about 12% and other uncertainties are negligible.

4. DISCUSSION

Filamentary molecular clouds and their relationship with star formation have been intensively studied over the past decades. Detailed case studies have revealed physical properties of a number of remarkable star-forming filaments such as Orion A Integral Shaped Filament (González Lobos, & Stutz 2019; Schleicher, & Stutz 2018), Nessie filament (Mattern et al. 2018), SDC13 (Williams et al. 2018; McGuire et al. 2016). These filaments exhibit complex gas kinematics, and often appear to be highly fragmented along their major axes.

On the other hand, tenuous filaments are often found to be connected with large angles or orthogonal to the massive and star-forming filaments. For example H12 reported several filamentary streamers converge to the DR21(OH) with their column densities about a few orders of magnitude lower than that of the DR 21 ridge. Being a part of the giant filamentary network, DR21SF has a length about 4 pc, comparable with that of massive star-forming filaments, but it is significantly less active in star formation. While, DR21SF is apparently thicker and more massive than the minor and tenuous gas flows connected to the DR21(OH) ridge (sub-filament F1, F2 and F3 for example, see Table 1 of H12 for a comparison).

So, what is the nature of DR21SF? Is it a stable structure that is capable of forming stars in itself? What is the physical connection between DR21SF and the massive young stars in DR 21? These questions are of great interests to our understanding of the star formation ac-

tivity in Cygnus X and the dynamical evolution of dense molecular cloud filaments.

4.1. *Star Formation and Stability*

Thanks to the deep and unbiased infrared surveys towards Cygnus X carried out with Balloon-borne Large Aperture Sub-millimeter Telescope (BLAST, Roy et al. 2011), *Herschel* Space Telescope and *Spitzer* Space Telescope, we are able to search deep embedded young stellar objects (YSOs) and compact clumps which can potentially form stars along the filament. We find signposts of star formation at P03, P07 and P10, in the surveys mentioned above. As shown in Figure 1, two compact mid-infrared (MIR) objects are detected at P03 by the *Spitzer* Space Telescope, and later recognized as Class I low-mass YSO candidates by SED fitting using *Spitzer*, UKIDSS and 2MASS data (Kryukova et al. 2014). With luminosities about $505 L_{\odot}$ and $86 L_{\odot}$, they are found to be coincident with an “IR-quiet”² massive dense core (MDC, named as DR21-22 by Cao19) with a mass of $36.5 M_{\odot}$. The MDC shows no evidence of high mass star formation according to its IR luminosity. The two objects are likely to be clusters of or individual intermediate-/low-mass forming stars. At P07, a sub-mm object J203914+421221 is detected by Roy et al. (2011) with BLAST. By the SED fitting of sub-mm and FIR data (500, 350, 250, 100, and 60 μm), the authors infer this object to be a pre-stellar massive ($80 M_{\odot}$) clump at its very early stage with a total luminosity of $270 L_{\odot}$ and a temperature 20.2 K. However, in a search of dense clumps with a mass completeness level of $35 M_{\odot}$ by Cao19, no clump is detected at this position. The inconsistency may come from distinct data reduction procedures and spatial

resolutions. As argued by Cao19, the source extraction process is highly effected by the background diffuse emission removal, thus different background removal algorithms may result in different detection. Also, the image resolution of Cao19 (20'') is significantly higher than that of Roy et al. (2011) (1'), so the clump recognized by the latter may be resolved into several less massive objects or relatively extended structures. We also found two Class I YSOs with very low luminosities of $0.7 L_{\odot}$ and $1.5 L_{\odot}$ at P10. The less luminous one shows much more flatter SED with spectral index of $\alpha = 0.21$ than that of the other YSO $\alpha = 1.67$. Greene et al. (1994) referred such objects as “flat spectrum” since their evolutionary stages show ambiguity between Class I and Class II, and may statistically infer a later evolutionary status than typical Class I YSOs. Makin & Froebrich (2018) carried out a 2.122 μm molecular hydrogen line survey of jets and outflows from young stars covering the whole Cygnus X complex as part of the UWISH2 survey. The 2.122 μm molecular hydrogen emission line is excited by the shocks that produced by the high velocity outflow impacting the surrounding molecular gas. We find no detection of 2.122 μm molecular hydrogen emission towards all the YSOs identified in DR21SF in this survey. This is an indicator that the YSOs in DR21SF lack collimated jets, and may have only produced large angle outflows that are not able to generate strong enough shocks in the natal clouds.

The NH_3 observations (Table 1) show that the gas temperatures at P02, P03, P07, P08 and P10 are significantly higher than typical temperatures (10 - 15 K) of cold molecular clouds. This can be explained by the objects we have found at P03, P07 and P10, as the ongoing star-forming process will heat up the natal clouds. It is also a direct proof of that the YSOs or clumps found in these positions are physically associated, rather than only visually coincident,

² Cao19 defined “IR-quiet” MDCs as those with mid-IR flux lower than that of a B3-type stellar embryo, indicating the absence of high mass star formation in those cores.

with the filament. We find no YSO at P07, even though the gas temperature and line-width are higher than the rest parts of the filament. It is likely that the forming star or cluster is in its early evolutionary stage, so it may not be visible as a near-/mid-IR point source.

We then try to figure out that whether DR21SF is stable, or just a transient phenomenon, by investigating the stability using three time scales: life time, crossing time, and free-fall time. In the case of DR21SF, the YSOs identified in the filament are Class I objects. The age τ_i of such objects from pre-stellar to Class I stage is confined by $1 \text{ Myr} \leq \tau_i \leq 2 \text{ Myr}$ (Kirk et al. 2005; Evans et al. 2009). This will put a 1 Myr lower limit on the life time of the DR21SF. Recent observations towards many molecular cloud filaments appear to favor a turbulence supported gas cylinder scenario. At a temperature of 15 K, the thermal line-width is about 0.03 km s^{-1} for NH_3 , which is negligible compared to the measured line-widths in DR21SF. Therefore, we suggest that turbulence is the dominant supporting force in the case of DR21SF. Considering the 3D velocity dispersion $\sigma_{3D} = \sqrt{3}\sigma_{\text{aver}} = 2.5 \pm 0.9 \text{ km s}^{-1}$, where σ_{aver} is the average intrinsic line-width, the crossing time then can be derived as $t_{\text{cross}} = R/\sigma_{3D} = 7.8 \times 10^4 \text{ yr}$, in a turbulence supported case. The free-fall time of DR21SF can be estimated as $t_{\text{ff}} = \sqrt{3\pi/32G\rho} = 1.3 \times 10^5 \text{ yr}$, where ρ is the average volume density. Both t_{cross} and t_{ff} are about an order of magnitude smaller than the lower limit of the age of the filament. This indicates that DR21SF is a stable structure rather than a transient concentration of the ISM. However, the crossing time is significantly smaller than the free-fall time. This is a clear sign that the self-gravity of the filament is not strong enough to overcome the turbulent pressure and the filament would have been dispersed by the strong turbulence. To solve this

contradiction, we then have to look into the stability status of the filament.

According to Fiege & Pudritz (2000) the linear virial mass of turbulence supported filaments is given by

$$(M/l)_{\text{vir}} = 2\sigma^2/G = 84\left(\frac{\sigma_{3D}}{\text{kms}^{-1}}\right)^2 M_{\odot}\text{pc}^{-1}. \quad (5)$$

We calculate the virial mass using the equation above and the mass using the same method as the total mass estimation, for each of the 10 segments along the filament at P01 to P10. The virial parameter of each segment listed in Table 2 is the ratio of these two values. The virial parameter along the filament is mostly around 1 to 2, suggesting that DR21SF is overall in a trans-critical status, that the gravity and turbulent pressure rival each other. At P02, and P04, the virial parameters are significantly larger than 2. Since YSOs have already been identified at this area, the large virial parameters do not really reflect stronger turbulence. Instead, the feedback of the star formation activities, such as large angle outflows, may introduce perturbation to the surrounding molecular clouds and increase the line-width. The large virial parameter at P07 and P10, comparing to their neighbor segments, can also be explained by the similar effect. This could be another evidence of the unseen star formation activities at extremely early stage at P07, independent from the temperature excess. We notice that the tail of filament is in a supercritical status indicated by the small virial parameters. This is usually a reflection of effective collapse of the cloud under its self-gravity, and can possibly explain the later evolutionary stage of one of the YSOs identified at P10.

The magnetic field also plays an important role in shaping filamentary molecular clouds by providing the supporting force against the gravity or directing the mass accretion flow (Hennebelle & Inutsuka 2019). Supercritical filaments are usually observed to be perpendicular

Table 2. The virial parameter of 10 segments along the DR21 south filament.

Segment	M_{vir}	M	α
	M_{\odot}	M_{\odot}	
P01	314	169	1.9
P02	592	114	5.2
P03	256	108	2.4
P04	323	110	2.9
P05	131	97	1.3
P06	94	93	1.0
P07	183	89	2.0
P08	62	91	0.7
P09	55	93	0.6
P10	85	83	1.0

to the magnetic fields (Lee et al. 2017), whereas the striations that are attached to the main filaments are highly elongated along the B-field (Heyer et al. 2016). In the case of DR 21, the large scale magnetic field runs almost perpendicular to the north-south main ridge consisting of DR 21 and DR21(OH) (e.g. Kirby 2009). The accretion flow onto the DR21(OH) through the sub-filaments F3, on the other hand, has been reported being parallel to the magnetic field (Schneider et al. 2010). We illustrate the large scale magnetic field orientation around DR 21 derived by Planck dust continuum polarization data³ in Figure 1. DR21SF is mostly aligned along the large scale magnetic field, and is more consistent with the scenario that DR21SF is overall a large scale accretion flow. Even though in theory, the length scale of “sausage” fragmentation is maintained with the presence of a magnetic field parallel to the filament (Nagasawa 1987), we do not see such a fragmentation occurs in DR21SF as it does in many su-

percritical filaments. At the northern end of DR21SF, where the two YSO candidates are found, the magnetic field bends to form a large angle with the spine of the filament. With the limited resolution of Planck data, it is difficult to tell whether this alteration of the magnetic field orientation is caused by the star formation in DR21SF or by the influence of DR 21, where strong magnetic field almost perpendicular to the ridge is seen. High resolution observations of the dust polarization towards DR21SF could help us to obtain a better understanding of the stability status of DR21SF.

How will such a filament dynamically evolve? Gong et al. (2018) compared two star-forming filaments with similar mass and distinct central density, Serpens filament and Serpens south filament. They infer that the slightly supercritical filament (Serpens filament) with lower central density and weaker signature of radial collapse is on an earlier evolutionary stage prior to the other’s (Serpens south filament), which is consistent with the relatively inactive status of Serpens filament in star formation. From a theoretic respect Inutsuka & Miyama (1992) proposed that the radial collapse starts in an isothermal gas cylinder when the linear mass is greater than the critical value, and accelerates until the central density increase and the equation of state varies much from the isothermal one, then the filament may finally fragment. In other words, in a filament in its early evolutionary stage, the radial collapse dominates over the fragmentation. DR21SF shows significantly lower central density compared with other star-forming filaments (see Table 3 in Gong et al. 2018), which may indicate an early evolutionary stage. This is confirmed by the detection of sparse YSOs in DR21SF. Thus the theory by Inutsuka & Miyama (1992) can be a possible explanation of the coherent profile of DR21SF. However, direct observational evidences of ra-

³ <https://pla.esac.esa.int/>

dial collapse are in need to verify this hypothesis in DR21SF.

DR21SF seems to be quiescent since we find no signpost for massive star formation (e.g., H II regions or Class II methanol masers) and see only two sites of low-/intermediate-mass YSOs (P03 and P10) along the filament with no energetic feedbacks (e.g., shocks produced by jets or outflows). Whereas the star formation sites in other sub-filaments connecting to DR21(OH) are more active with the detection of outflows (see Figure 1 for a comparison). There are other filamentary objects which are similar to DR21SF in terms of stability status. In the Galactic central molecular zone (CMZ), filaments are often being massive and quiescent at the same time due to the intensive turbulence. For example the G0.253+0.016 cloud (the ‘‘Brick’’) is a turbulence dominated filamentary system located in CMZ, with a mass of $7.2 \times 10^4 M_{\odot}$, and an apparent size of 17 pc^2 , and only two dense core candidates and one H₂O maser are detected (Federrath et al. 2016; Rathborne et al. 2014, and references therein). However, the physical condition of CMZ is apparently more extreme than that of DR21SF. The gas temperature is up to 100 K and one dimensional Mach number in CMZ is 30 (Rathborne et al. 2014), which are significantly higher than those in DR21SF. Federrath et al. (2016) claimed that the solenoid driving caused by shearing motions in CMZ is the dominant turbulence driving model in G0.253+0.016, which reduces the star formation rate compared to typical clouds in solar neighborhood. In our case, the strong gravitational field produced by DR 21 may be a potential engine of compressing driving turbulence.

4.2. A Scenario of Gas In-falling of DR21SF

There are in principle three possible interpretations of the radial velocity gradient along filamentary molecular clouds: rotation, outflow, or in-fall. The rotation scenario is unrealistic since

the centrifugal force needed to maintain the 3.6 pc filament is too dramatic. Considering an outflow scenario, we assume that the filament is a mass ejection originating from DR 21. In this case, stellar winds or jets would be the most likely candidate sources for driving the outflow motions. However, DR 21 is already harboring one of the most luminous and largest warm (2000 K) bipolar outflows in the Galaxy (Garden et al. 1986). There is not any star formation theory that could provide a feasible interpretation of two such large outflows, one warm and bipolar and the other cold and unipolar, coming from a cluster of UC H II regions. Since neither the rotation nor the outflow scenario appears to be feasible, we propose that the radial velocity gradient of DR21SF is produced by an accelerating in-fall along the filament. The gas flows from the south to the north along DR21SF, induced by the gravitational field of DR 21. Arzoumanian et al. (2013) proposed that in this process the radially collapsing filaments will keep a constant width along their spine. This is also in agreement with our observation.

The system consisting of DR21SF and DR 21 seems to be quite similar to the ‘‘head-tail’’ system reported by Tachihara et al. (2002), in which the ‘‘head’’ is an active massive star forming region with a high column density and the much less dense ‘‘tail’’ often shows only signposts of low-mass star formation. Tachihara et al. (2002) claimed that in the ‘‘head-tail’’ scenario, stellar winds from other OB stars in the opposite position of the ‘‘tail’’ are likely to be the trigger of the formation of the cometary structure. We believe in DR21SF this is not likely to be the case, since the massive star-forming site to the north, DR21(OH), is still at an early evolutionary stage and the radiation and winds from embedded high-mass protostars not yet expel surrounding molecular clouds. Therefore they are not expected to pro-

duce a “head-tail” scenario at DR 21. Thus the DR21SF-DR 21 system looks similar to a “head-tail” picture, but the system is not induced by nearby OB stars, and the “tail” is an accretion flow onto the “head”.

Because of the conservation of the total energy during the accelerating in-fall, one can estimate the inclination angle of the filament by analyzing its energy budget, assuming the a free-fall gas cylinder model. With an inclination angle θ , with respect to the plane of sky, the first order estimate of the total energy of the in-fall gas in a unit volume reads

$$E_{\text{prot}} + E_{\text{kin}} + E_{\text{turb}} + E_{\text{therm}} = C, \quad (6)$$

where $E_{\text{prot}} = \frac{Gm_i m_{\text{DR21}} \cos \theta}{r_i}$ is the gravitational energy of gas with mass M_i at projected distance r_i to DR 21 in the plane of sky, $E_{\text{kin}} = m_i \frac{v_{\text{LSR}}^2}{\sin^2 \theta}$ is the kinetic energy with relative radial velocity v_{LSR} in respect of the southern end of DR21SF, and $E_{\text{turb}} + E_{\text{therm}} = m_i \Delta v^2$ is the internal energy (including thermal and turbulent components) with Δv being the intrinsic line-width of the gas. The local mass is defined as $m_i = P_i \cos \theta / w$, where P_i is the local column density, and $w = 0.13$ pc is the width of DR21SF. We again use the column density, radial velocity and intrinsic line-width from P03 to P09 to fit the model. The best-fit model is illustrated in Figure 5, which gives an estimate of the inclination angle of 18° . Thus the projection effect is insignificant in the analysis of DR21SF. Kirby (2009) estimated the inclination angle of the DR 21 main ridge is about 20° to the plane of the sky by fitting line-width ratio of emissions from neutral molecules and ions in the magnetic field. This result is in good agreement with ours.

We then give an estimate of the mass in-fall rate of DR21SF with the assumption of a homogeneous cylinder(Peretto et al. 2014):

$$\dot{M} = \pi(w/2)^2 \rho V = \frac{M}{L} V, \quad (7)$$

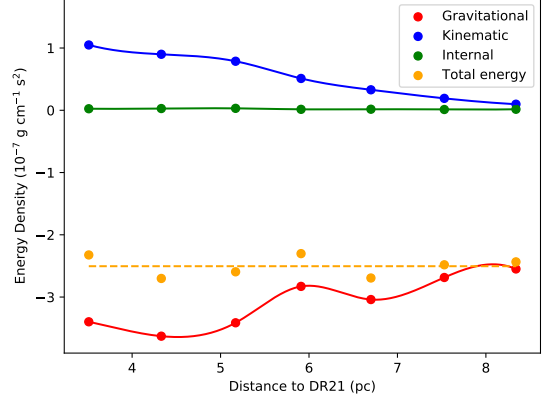


Figure 5. The gravitational energy, kinematic energy and internal energy of gas in an unit volume at P03, P04, P05, P06, P07, P08, and P09 are denoted by red, blue, and green dots, respectively, with spline interpolation to give a rough impression of how the energies are distributed along the DR21SF. The yellow dots illustrate the total energy given by the best-fit. The yellow dashed horizontal line is a linear fit of the total energy showing the total energy preserves along the filament.

in which w is the width of the filament, ρ is the average density, V is the in-fall velocity at the northern end of the filament, where we adopt the velocity of P01, M is the total mass, and L is the length of the filament. The in-fall velocity can be estimated by radial velocities as $V_{\text{infall}} = (V_{\text{P01}} - V_{\text{DR21}}) / \sin \theta = 3.7 \text{ km s}^{-1}$, where $V_{\text{DR21}} = -3.0 \text{ km s}^{-1}$. Thus the mass in-fall rate is $\dot{M} = 1.1 \times 10^{-3} M_{\odot} \text{ yr}^{-1}$. Our estimate is about two orders of magnitude larger than the estimate of the mass in-fall rate of SDC13 filament ($2.5 \times 10^{-5} M_{\odot} \text{ yr}^{-1}$, Peretto et al. 2014), and is similar to that of F3 filament onto the DR21(OH) clump ($1.9 \times 10^{-3} M_{\odot} \text{ yr}^{-1}$, Schneider et al. 2010), which is believed to contribute about one third of the total mass in-fall rate of the clump. Since there is no detected gas flow towards DR 21 along the DR21 ridge (Schneider et al. 2010), the gas in-fall along the DR21SF is possibly the most important, if not only, accretion flow that is feeding DR 21 massive star forming region.

5. SUMMARY

DR21SF is a massive filament distinct from the major star-forming filaments or the low-density striations associated with the major filaments. Based on the column density map derived from *Herschel* images, we find that DR21SF is a coherent filament with no clear signs of fragmentation, but still hosting star formation activities. Several low-/intermediate-mass YSOs are identified in the filament, with one candidate of star forming core in its extremely early evolutionary stage. The temperature, optical depth, radial velocity, and the velocity dispersion of the filament is derived by $\text{NH}_3(1, 1)$ and $(2, 2)$ emission line observations. With a size of 3.6 pc by 0.13 pc and a mass of $1048 M_\odot$, The filament has an average temperature typical of cold molecular clouds, but the sites of low-/intermediate-mass YSOs show temperature excess. The lack of signatures of fragmentation in DR21SF, compared to other filaments in the Cygnus X north filamentary network, may be due to the early evolutionary stage or the unique external gravitational field produced by DR 21.

A radial velocity gradient of $0.8 \text{ km s}^{-1} \text{ pc}^{-1}$ is detected along the spine of DR21SF. We in-

terpret these gradients with a scenario of an accelerating gas flow in DR21SF towards DR 21, with a mass transfer rate of $1.1 \times 10^{-3} M_\odot \text{ yr}^{-1}$. We also proposed an energy-budget method to estimate the inclination angle of the filament under the assumption of such a scenario. Our observations shed new lights on the filament network around DR 21, and provide hints that the source of the most energetic outflow in our Galaxy may have a major mass supply from a parsec scale accretion flow.

ACKNOWLEDGMENTS

B.H., K.Q., Y.C., J.L., Y.W., and J.W. are supported by National Key R&D Program of China No. 2017YFA0402600. We acknowledge the support from National Natural Science Foundation of China (NSFC) through grants No. U1731237, 11473011, 11590781, 11629302, 11590780, 11590784, 12073064, and the Scientific Program of Shanghai Municipality (08DZ1160100).

Facilities: TianMa Radio Telescope (TMRT)

Software: Astropy (Astropy Collaboration et al. 2013), GILDAS

REFERENCES

- André, P., Men'shchikov, A., Bontemps, S., et al. 2010, *A&A*, 518, L102
- Arzoumanian, D., André, P., Didelon, P., et al. 2011, *A&A*, 529, L6
- Arzoumanian, D., André, P., Peretto, N., & Könyves, V. 2013, *A&A*, 553, A119
- Astropy Collaboration, Robitaille, T. P., Tollerud, E. J., et al. 2013, *A&A*, 558, A33
- Bally, J., Langer, W. D., Stark, A. A., & Wilson, R. W. 1987, *ApJL*, 312, L45
- Barranco, J. A., & Goodman, A. A. 1998, *ApJ*, 504, 207
- Cao, Y., Qiu, K., Zhang, Q., et al. 2019, *The Astrophysical Journal Supplement Series*, 241, 1
- Ching, T.-C., Lai, S.-P., Zhang, Q., et al. 2017, *ApJ*, 838, 121
- Cyganowski, C. J., Reid, M. J., Fish, V. L., & Ho, P. T. P. 2003, *ApJ*, 596, 344
- Davis, C. J., Kumar, M. S. N., Sandell, G., et al. 2007, *MNRAS*, 374, 29
- Evans, N. J., II, Dunham, M. M., Jørgensen, J. K., et al. 2009, *ApJS*, 181, 321
- Federrath, C., Rathborne, J. M., Longmore, S. N., et al. 2016, *ApJ*, 832, 143
- Fiege, J. D., & Pudritz, R. E. 2000, *MNRAS*, 311, 85
- Garden, R., Geballe, T. R., Gatley, I., & Nadeau, D. 1986, *MNRAS*, 220, 203

- Gong, Y., Li, G. X., Mao, R. Q., et al. 2018, *A&A*, 620, A62
- González Lobos, V., & Stutz, A. M. 2019, *MNRAS*, 489, 4771
- Greene, T. P., Wilking, B. A., Andre, P., et al. 1994, *ApJ*, 434, 614. doi:10.1086/174763
- Harvey-Smith, L., Soria-Ruiz, R., Duarte-Cabral, A., & Cohen, R. J. 2008, *MNRAS*, 384, 719
- Hennebelle, P. & Inutsuka, S.-. ichiro . 2019, *Frontiers in Astronomy and Space Sciences*, 6, 5
- Hennemann, M., Motte, F., Schneider, N., et al. 2012, *A&A*, 543, L3
- Henning, T., Linz, H., Krause, O., et al. 2010, *A&A*, 518, L95
- Heyer, M., Goldsmith, P. F., Yıldız, U. A., et al. 2016, *MNRAS*, 461, 3918
- Ho, P. T. P., & Townes, C. H. 1983, *ARA&A*, 21, 239
- Inutsuka, S.-I., & Miyama, S. M. 1992, *ApJ*, 388, 392
- Jackson, J. M., Finn, S. C., Chambers, E. T., Rathborne, J. M., & Simon, R. 2010, *ApJL*, 719, L185
- Jakob, H., Kramer, C., Simon, R., et al. 2007, *A&A*, 461, 999
- Johnstone, D., & Bally, J. 1999, *ApJL*, 510, L49
- Kirby, L. 2009, *ApJ*, 694, 1056. doi:10.1088/0004-637X/694/2/1056
- Kirk, J. M., Ward-Thompson, D., & André, P. 2005, *MNRAS*, 360, 1506
- Kirk, H., Myers, P. C., Bourke, T. L., et al. 2013, *ApJ*, 766, 115
- Kogan, L., & Slysh, V. 1998, *ApJ*, 497, 800
- Kryukova, E., Megeath, S. T., Hora, J. L., et al. 2014, *AJ*, 148, 11
- Lee, Y.-N., Hennebelle, P., & Chabrier, G. 2017, *ApJ*, 847, 114
- Liu, H. B., Jiménez-Serra, I., Ho, P. T. P., et al. 2012, *ApJ*, 756, 10
- Lu, X., Zhang, Q., Liu, H. B., Wang, J., & Gu, Q. 2014, *ApJ*, 790, 84
- Lu, X., Zhang, Q., Liu, H. B., et al. 2018, *ApJ*, 855, 9
- Makin, S. V., & Froebrich, D. 2018, *ApJS*, 234, 8
- Mattern, M., Kainulainen, J., Zhang, M., et al. 2018, *A&A*, 616, A78
- McGuire, C., Fuller, G. A., Peretto, N., et al. 2016, *A&A*, 594, A118
- Miville-Deschênes, M.-A., Martin, P. G., Abergel, A., et al. 2010, *A&A*, 518, L104
- Motte, F., Bontemps, S., Schilke, P., et al. 2007, *A&A*, 476, 1243
- Myers, P. C. 2009, *ApJ*, 700, 1609
- Nagasawa, M. 1987, *Progress of Theoretical Physics*, 77, 635. doi:10.1143/PTP.77.635
- Ostriker, J. 1964, *ApJ*, 140, 1056
- Peretto, N., Fuller, G. A., Duarte-Cabral, A., et al. 2013, *A&A*, 555, A112
- Peretto, N., Fuller, G. A., André, P., et al. 2014, *A&A*, 561, A83
- Rathborne, J. M., Longmore, S. N., Jackson, J. M., et al. 2014, *ApJL*, 795, L25
- Rohlfs, K., & Wilson, T. L. 2004, *Tools of radio astronomy*, 4th rev. and enl. ed., by K. Rohlfs and T.L. Wilson. Berlin: Springer, 2004
- Roy, A., Ade, P. A. R., Bock, J. J., et al. 2011, *ApJ*, 727, 114
- Rygl, K. L. J., Brunthaler, A., Sanna, A., et al. 2012, *A&A*, 539, A79
- Schleicher, D. R. G., & Stutz, A. 2018, *MNRAS*, 475, 121
- Schneider, S., & Elmegreen, B. G. 1979, *ApJS*, 41, 87
- Schneider, N., Bontemps, S., Simon, R., et al. 2006, *A&A*, 458, 855
- Schneider, N., Csengeri, T., Bontemps, S., et al. 2010, *A&A*, 520, A49
- Tachihara, K., Onishi, T., Mizuno, A., et al. 2002, *A&A*, 385, 909
- Walmsley, C. M., & Ungerechts, H. 1983, *A&A*, 122, 164
- Williams, G. M., Peretto, N., Avison, A., et al. 2018, *A&A*, 613, A11